

UC Berkeley

UC Berkeley Previously Published Works

Title

1D Magnetic MX₃ Single-Chains (M = Cr, V and X = Cl, Br, I)

Permalink

<https://escholarship.org/uc/item/37p165ng>

Journal

Advanced Materials, 35(49)

ISSN

0935-9648

Authors

Lee, Yangjin

Choi, Young Woo

Lee, Kihyun

et al.

Publication Date

2023-12-01

DOI

10.1002/adma.202307942

Copyright Information

This work is made available under the terms of a Creative Commons Attribution License, available at <https://creativecommons.org/licenses/by/4.0/>

Peer reviewed

1D Magnetic MX_3 Single-Chains ($\text{M} = \text{Cr}, \text{V}$ and $\text{X} = \text{Cl}, \text{Br}, \text{I}$)

Yangjin Lee, Young Woo Choi, Kihyun Lee, Chengyu Song, Peter Ercius, Marvin L. Cohen, Kwanpyo Kim,* and Alex Zettl*

Magnetic materials in reduced dimensions are not only excellent platforms for fundamental studies of magnetism, but they play crucial roles in technological advances. The discovery of intrinsic magnetism in monolayer 2D van der Waals systems has sparked enormous interest, but the single-chain limit of 1D magnetic van der Waals materials has been largely unexplored. This paper reports on a family of 1D magnetic van der Waals materials with composition MX_3 ($\text{M} = \text{Cr}, \text{V}$, and $\text{X} = \text{Cl}, \text{Br}, \text{I}$), prepared in fully-isolated fashion within the protective cores of carbon nanotubes. Atomic-resolution scanning transmission electron microscopy identifies unique structures that differ from the well-known 2D honeycomb lattice MX_3 structure. Density functional theory calculations reveal charge-driven reversible magnetic phase transitions.

1. Introduction

Magnetism at surfaces, interfaces, and low-dimensional materials generally has long been of central interest for both fundamental research and technological advances.^[1] The reduced dimensionality often leads to strong spin fluctuations that affect magnetic ordering and give rise to a variety of novel magnetic phenomena^[2] including enhanced magnetic anisotropy. These characteristics underpin device applications such as magnetic storage, spintronics, and magnetic sensing.^[1a,g] Recent discoveries of intrinsic magnetism in 2D van der Waals materials have intensified the search for new atomically thin magnetic materials, and single 2D layers of CrI_3 ,^[1e] $\text{Cr}_2\text{Ge}_2\text{Te}_6$,^[1c] FePS_3 ,^[3] VSe_2 ,^[4] and MnSe_2 ^[5] are prime

examples. However, there has been limited exploration of other dimensional polymorphs, particularly 1D chain structures. Moreover, although some quasi-1D magnetic materials have received modest attention, the synthesis of fully isolated, truly 1D single-chain magnets has proven difficult. In a promising recent advancement,^[6] some single CrCl_3 chains were observed amongst collections of multi-chain CrCl_3 bundles grown on NbSe_2 substrates. Synthesis and further experimental studies of such structures are exceedingly challenging because of the sensitivity of halide materials to light, oxygen, and moisture.^[7]

One promising method for fabricating and enabling further characterization of sensitive 1D structures is to employ hollow-core nanotubes as nano-reaction vessels. Carbon nanotubes (CNTs) and boron nitride nanotubes (BNNTs) have facilitated synthesis of various materials, including monoelements,^[8] metal halides,^[9] chalcogenides,^[10] and perovskites.^[11] The geometrical-confinement effect imposed by the cavities inside the nanotube can lead to the formation of crystal structures and morphologies that are unknown in bulk counterparts.^[10d,e,g,k] A small inner diameter nanotube can favor 1D structures, as it constrains the radial dimension for the encapsulated material.^[9b,10k] The use of nanotube sheaths provides protection against oxidation and enables experimental study of 1D nanostructures that are not air-stable.^[9b,10g] Furthermore, especially in the case of CNT encapsulation, possible charge transfer between the CNT and the core chain provides an additional control parameter for altering material properties.

Here, we report the creation and study of a family of 1D magnetic van der Waals single-chains of MX_3 ($\text{M} = \text{Cr}, \text{V}$ and $\text{X} = \text{Cl}, \text{Br}, \text{I}$), fully isolated within the cores of CNTs. Nanotube encapsulation enables stabilization of the structure of the 1D

Y. Lee, Y. W. Choi, M. L. Cohen, A. Zettl
Department of Physics
University of California at Berkeley
Berkeley, CA 94720, USA
E-mail: azettl@berkeley.edu


Y. Lee, Y. W. Choi, M. L. Cohen, A. Zettl
Materials Sciences Division
Lawrence Berkeley National Laboratory
Berkeley, CA 94720, USA

Y. Lee, K. Lee, K. Kim
Department of Physics
Yonsei University
Seoul 03722, South Korea
E-mail: kpkim@yonsei.ac.kr

Y. Lee, K. Lee, K. Kim
Center for Nanomedicine
Institute for Basic Science
Seoul 03722, South Korea

C. Song, P. Ercius
National Center for Electron Microscopy, The Molecular Foundry
Lawrence Berkeley National Laboratory
Berkeley, CA 94720, USA

A. Zettl
Kavli Energy NanoSciences Institute
University of California at Berkeley
Berkeley, CA 94720, USA

 The ORCID identification number(s) for the author(s) of this article can be found under <https://doi.org/10.1002/adma.202307942>

© 2023 The Authors. Advanced Materials published by Wiley-VCH GmbH. This is an open access article under the terms of the Creative Commons Attribution License, which permits use, distribution and reproduction in any medium, provided the original work is properly cited.

DOI: 10.1002/adma.202307942

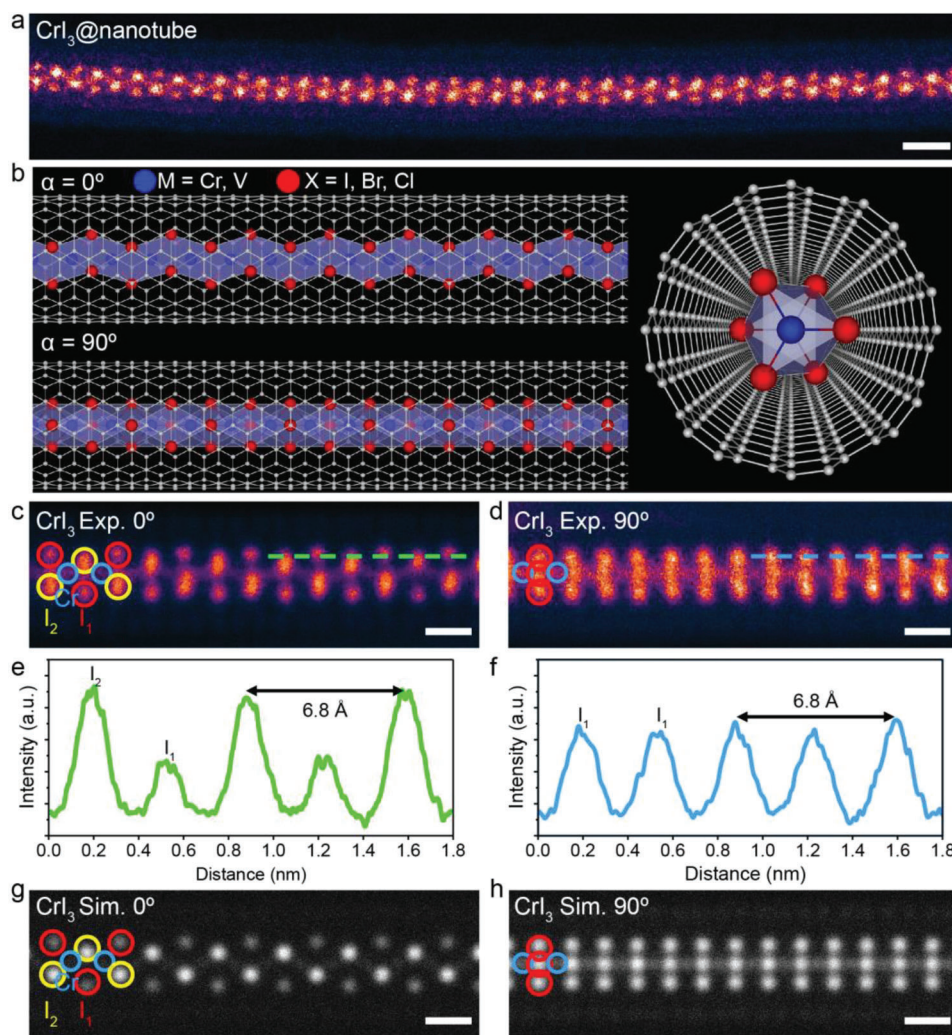


Figure 1. Structure characterization of 1D CrI_3 single-chain inside a nanotube. a) Aberration-corrected ADF-STEM image of a CrI_3 single-chain encapsulated within a double-walled CNT. Scale bar: 1 nm. b) Atomic model of face-sharing 1D MX_3 single-chain within nanotube. The face-sharing MX_6 octahedra are shadowed. The transition metal atoms are displayed in blue and the halogen atoms are displayed in red. c,d) Experimentally observed atomic-resolution STEM images of c) 0° and d) 90° rotated CrI_3 single chains encapsulated inside nanotubes. Cr, I_2 , and I_1 are marked by blue, yellow, and red circles, respectively. Scale bar: 0.5 nm. e,f) Intensity line profile along the colored line in panels (c) and (d), respectively. g,h) Simulated STEM images of g) 0° and h) 90° rotated CrI_3 single chains encapsulated inside nanotubes. Cr, I_2 , and I_1 are marked by blue, yellow, and red circles, respectively. Scale bar: 0.5 nm.

MX_3 single-chains, and simultaneously prevents environmental degradation, facilitating detailed structural characterization. Atomic-resolution scanning transmission electron microscopy (STEM) imaging and simulation clearly identify the 1D MX_3 chain configurations. The 1D MX_3 chains consist of face-sharing MX_6 octahedra, in distinct contrast to the edge-sharing octahedral found in the complementary 2D honeycomb lattice MX_3 structure. Density functional theory (DFT) calculations reveal that a significant fraction of electronic charges is transferred from the CNTs to the chain. The electron transfer stabilizes the face-sharing single-chain structure against the edge-sharing layered structure, and strongly affects the magnetic energies of the chains. Notably, CrX_3 chains tend to undergo antiferromagnetic (AFM) to ferromagnetic (FM) transitions as a function of electron doping.

2. Results and Discussion

CrI_3 chains are directly synthesized by vacuum annealing CrI_3 precursors in the presence of open-ended nanotubes at high temperatures (see Experimental Section for the details). The samples are primarily screened using transmission electron microscopy (TEM) to confirm that the target material has successfully filled inside the nanotubes. The atomic structure of the filled material is further investigated using annular dark field (ADF) aberration-corrected STEM.

Figure 1a shows an atomic-resolution ADF-STEM image of a 1D CrI_3 single-chain encapsulated within a nanotube with an inner diameter of 1.1 nm. The CrI_3 chain encapsulated nanotubes are filled to around 90% with chain length of several hundred nanometers (Figure S1, Supporting Information). The

composition ratio of the encapsulated CrI_3 is determined by energy-dispersive spectroscopy (EDS), which confirms a composition 25.4 ± 2.8 atomic percent (atom%) Cr and 74.6 ± 3.6 atom%, yielding an atomic ratio $X/M = 2.9$ (expected ratio = 3). The ADF-STEM image contrast strongly depends on the atomic number (Z) which allows direct distinguishing of Cr ($Z_{\text{Cr}} = 24$) from I ($Z_{\text{I}} = 53$). Our DFT binding energy calculations (Figure S2, Supporting Information) show that CrI_3 single-chains are most stable when encapsulated within a nanotube of inner diameter 1.1 nm for both metallic armchair and semiconducting zigzag CNTs; this critical diameter is corroborated by our experimental observations for metallic CNTs.

Based on the observed STEM images, we find that the 1D CrI_3 chain structure consists of face-sharing CrI_6 octahedra along the chain axis (Figure 1b and Figure S3, Supporting Information). Figure 1c and d are magnified high-resolution (HR) ADF-STEM images at the different viewing directions (0° and 90° , respectively), which clearly show the atomic structure of 1D CrI_3 . Figure 1e,f shows intensity line profiles from the regions marked in Figure 1c,d, respectively. In the case of a 0° rotated image, the intensity difference of I_2 and I_1 along the chain direction is clearly distinguishable. The uniform intensities of I_1 are obtained from the 90° -rotated image. The lattice constant along the chain directions is 6.8 \AA from the observed images. The simulated STEM images are generated using the identified atomic structure, which match well with the experimentally observed results, as shown in Figure 1g,h.

The observed face-sharing in 1D CrI_6 octahedrons is different from that observed in the 2D CrI_3 counterpart. While the 2D CrI_3 also contains the same octahedrons, they are connected to each other in an edge-sharing mode to form a 2D honeycomb lattice (Figure S4, Supporting Information). Similar 1D face-sharing octahedral MX_3 chain structures are observed in other quasi-1D crystals such as $\beta\text{-TiCl}_3$ ^[12] and $\beta\text{-RuCl}_3$.^[13] We emphasize, however, that our observed 1D CrI_3 chain structure, and the isolation of this chain in a single-chain form, have not been previously reported. 2D CrI_3 often requires graphene or h-BN encapsulation for protection from ambient exposure or light-induced damages. We find that the synthesized CrI_3 chains inside nanotubes are stable under ambient exposure. The nanotube reaction vessel not only facilitates the formation of interesting structures but also provides an effective barrier against oxidation, as has been noted in prior research.^[9b,10g,11]

Extending the above findings for CrI_3 , we study the 1D MX_3 single-chain with different metal and halogen combinations. In our study we use in-house synthesized crystals of CrBr_3 and VI_3 , as well as commercially available powders of CrCl_3 , VBr_3 , and VCl_3 for MX_3 encapsulated nanotube fabrication (see Experimental Section for details). Figure 2 shows the experimental and simulated atomic-resolution STEM images of 0° -rotated MX_3 single-chains within the nanotube with different halogens and metals. All synthesized MX_3 single-chains inside the nanotube consist of face-sharing octahedral, identical to the CrI_3 case. The experimentally observed STEM images (left side) of CrBr_3 , VI_3 , and VBr_3 show similar image contrast to those of CrI_3 (Figure 2a,c,d) as here again the atomic numbers of the metals ($Z_{\text{V}} = 23$ and $Z_{\text{Cr}} = 24$) are lower than those of the corresponding halogens ($Z_{\text{I}} = 53$ and $Z_{\text{Br}} = 35$). In the case of CrCl_3 and VCl_3 , the atomic number of Cl ($Z_{\text{Cl}} = 17$) is lower than that of the metals, result-

ing in lower intensity compared to the metals (Figure 2b,e). The simulated STEM images (right side) of the MX_3 chain also show good agreement with the experimental results. The 90° -rotated simulated STEM images are shown in Figure S5, Supporting Information.

The measured lattice constants of the MX_3 chains along the chain direction are 6.3 \AA for CrBr_3 , 6.0 \AA for CrCl_3 , 6.8 \AA for VI_3 , 6.3 \AA for VBr_3 , and 6.0 \AA for VCl_3 , respectively (Figure S6, Supporting Information). The lattice constant of the MX_3 materials is primarily influenced by the halogen element rather than the transition metal. The size of the halogen ion affects the distance between neighboring atoms, which in turn affects the lattice constant. Transition metals, on the other hand, have a minor influence on the lattice constant of these materials. Our results strongly suggest that the face-sharing 1D MX_3 chain structures inside nanotubes can be stabilized universally in MX_3 compounds.

We now theoretically investigate the atomic, electronic, and magnetic properties of MX_3 single-chains by using first-principles DFT calculations. We first focus on isolated MX_3 single-chains with no surrounding nanotube. The atomic positions of isolated MX_3 single-chains are optimized by minimizing the total energy. The optimized lattice parameters are in excellent agreement with the experimental lattice parameters as shown in Table 1. For all MX_3 compounds, the MX_6 octahedra are elongated along the chain axis compared to the ideal octahedral structure. Although the elongation brings a small splitting of t_{2g} orbitals into a doubly-degenerate e_g^π and a nondegenerate a_{1g} orbital,^[14] three (two) t_{2g} electrons in Cr^{3+} (V^{3+}) magnetic ions remain fully spin-polarized to form $S = 3/2$ ($S = 1$) AFM (FM) chains (Figure 3a,b). CrCl_3 , CrBr_3 , and VI_3 have the easy axis perpendicular to the chain axis, and CrI_3 , VCl_3 , and VBr_3 parallel to the chain axis. For both Cr and V chains, the magnetic anisotropy is the strongest for chains with iodine. We note that the dependence of the magnetic anisotropy on the ligand atom is also pronounced in the monolayer CrX_3 , where the spin-orbit coupling of the ligand atom plays the dominant role in determining the magnetic anisotropy energy.^[15]

We now determine the magnetic exchange parameters of the 1D anisotropic Heisenberg model $H = \sum_{i < j} J_{ij}^{\parallel} S_i^{\parallel} S_j^{\parallel} + J_{ij}^{\perp} S_i^{\perp} \cdot S_j^{\perp}$, where S_i^{\parallel} and S_i^{\perp} are spin operators parallel and perpendicular to the easy axis, respectively, and J_{ij}^{\parallel} and J_{ij}^{\perp} are corresponding exchange interaction parameters. First, we obtain the density matrix of isolated MX_3 single-chains in vacuum including the spin-orbit interaction, and then the exchange parameters are calculated based on the magnetic force theorem.^[16] Figure S7, Supporting Information shows the calculated exchange interaction parameters as a function of distance between spins. We find that the magnetism of CrX_3 and VX_3 chains are of localized and itinerant character, respectively. For CrX_3 , the magnetic interactions are short-ranged and XXZ-type ($J_{ij}^{\parallel} \neq 0$). The dominant exchange parameters for CrX_3 are summarized in Table 1. On the other hand, VX_3 has oscillating and slowly decaying exchange interactions, which indicates itinerant magnetic interactions.

Figure S8, Supporting Information shows the calculated electronic structures of isolated nanotube-free MX_3 single-chains. Cr-based chains are insulating when in either an FM or AFM state. Interestingly, the conduction bands of CrX_3 chains in the

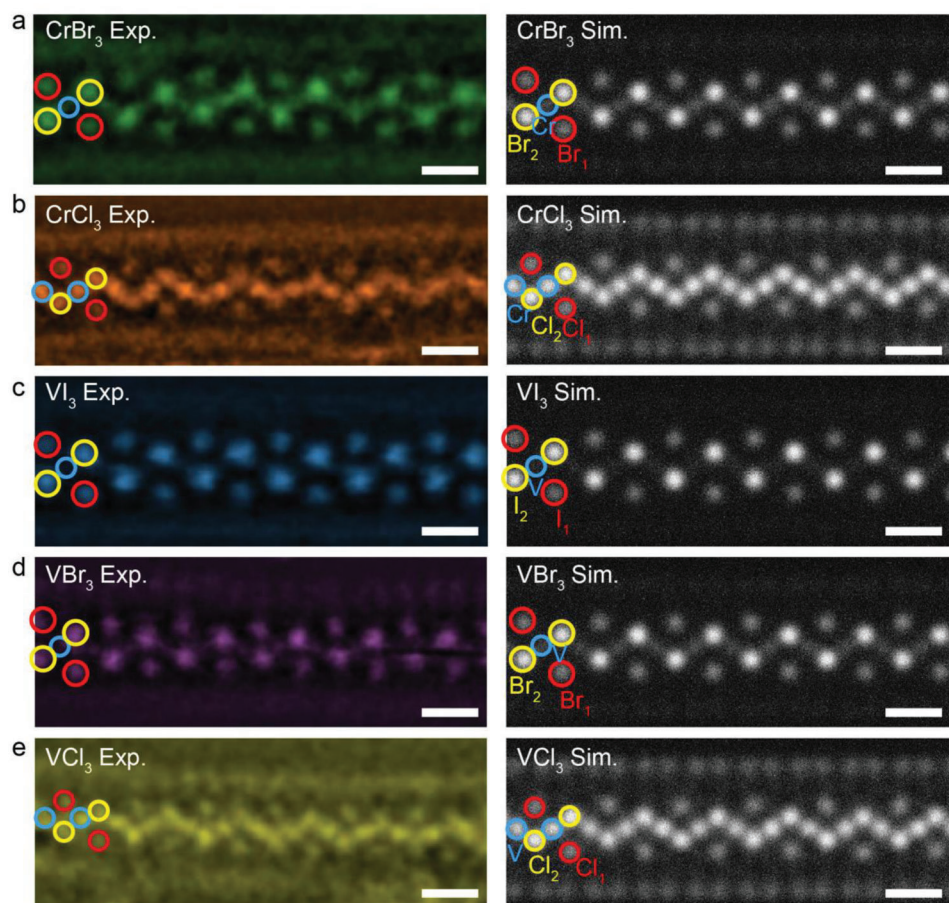


Figure 2. Universal stabilization of 1D MX_3 within a nanotube. a–e) Experimental (left) and simulated (right) atomic-resolution STEM images of a) CrBr_3 , b) CrCl_3 , c) VCr_3 , d) VBr_3 , and e) VCl_3 , respectively. Scale bar: 0.5 nm. The positions of transition metal atoms, halogen double atoms, and halogen single atoms are marked by blue, yellow, and red circles, respectively.

AFM phase are extremely flat and energetically well isolated. The narrow bandwidth can be understood as arising from kinetic frustration,^[17] where the direct hopping between Cr d orbitals destructively interferes with indirect hopping mediated by p orbitals in the halide atoms (see Figure S9, Supporting Information showing the conduction band wave functions). A related example is also pointed out in our recent study.^[10k] Since those conduction bands can be easily doped, for instance by electron transfer from a

CNT, we expect that the conduction bands of CrX_3 chains can provide an excellent platform to study correlated electron physics in 1D.^[2b] On the other hand, FM VX_3 chains are half-metals where majority spin states are metallic and minority spin states are insulating with a large band gap over 2 eV.

To illustrate the role of nanotube encapsulation, we examine theoretically MX_3 single-chains encapsulated within CNTs. Figure 3c,d shows that, because of the work function mismatch,

Table 1. Experimental (a_{exp}) and calculated lattice constants (a_{calc}) of MX_3 chains and DFT results of formation energies (E_f), easy axis, magnetic anisotropy energy (E_{MAE}), and magnetic exchange interaction parameters parallel ($J_{1,2}^{\parallel}$) and perpendicular ($J_{1,2}^{\perp}$) to the easy axis up to the second nearest neighbors.

	a_{exp} [Å]	a_{calc} [Å]	E_f [eV atom ⁻¹]	Easy axis	E_{MAE} [meV/f.u.]	$J_1^{\parallel}, J_2^{\parallel}$ [meV]	J_1^{\perp}, J_2^{\perp} [meV]
CrI_3	6.8	6.81 (FM) 6.72 (AFM)	-2.28	z	0.41	10.8, 5.3	3.1, -1.2
CrBr_3	6.3	6.29	-2.62	x	0.18	19.3, 4.0	9.0, -1.5
CrCl_3	6.0	6.00	-3.01	x	0.04	25.2, 3.0	15.0, -1.2
VI_3	6.8	6.69	-2.77	x	0.99	Itinerant ferromagnetism	
VBr_3	6.3	6.30	-3.18	z	0.20		
VCl_3	6.0	6.04	-3.60	z	0.28		

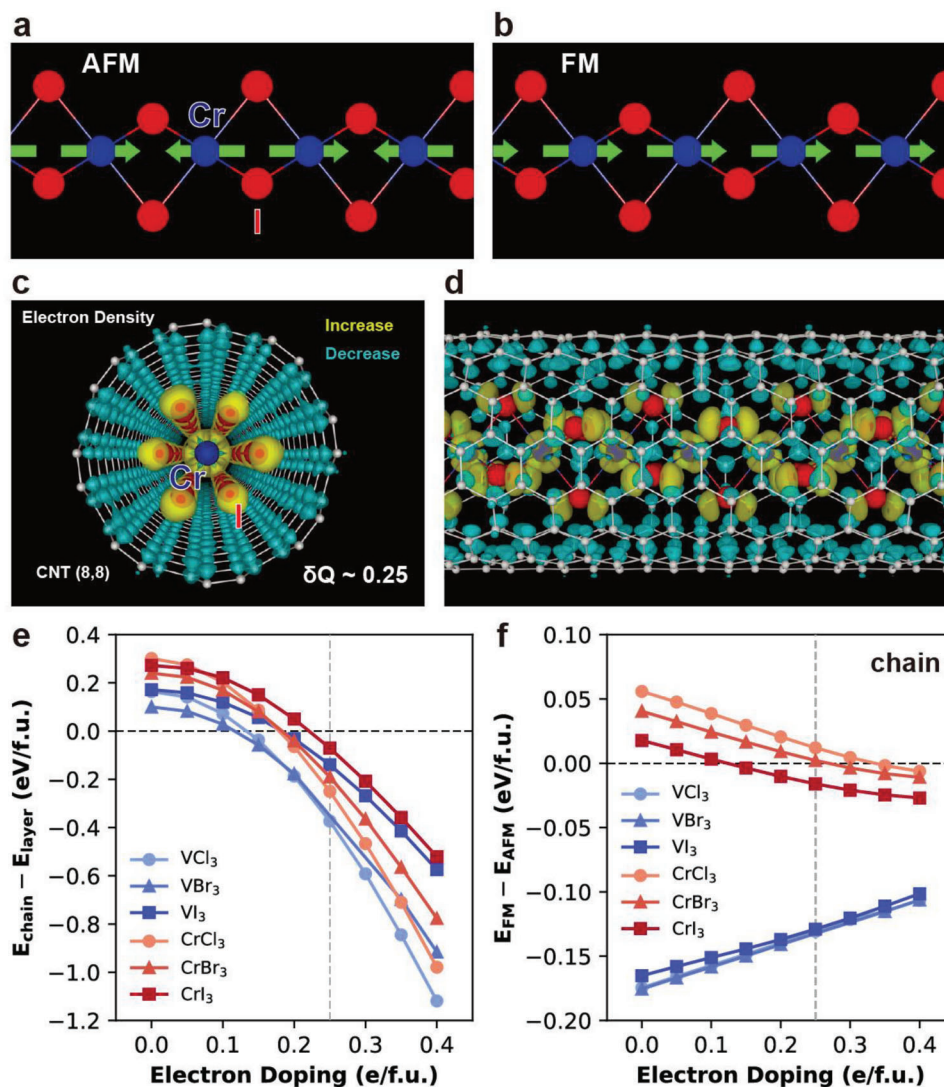


Figure 3. Calculated magnetic state, charge transfer from CNT, and electron doping effects. Schematics of a) antiferromagnetic and b) ferromagnetic state of CrI_3 single-chains. The easy axis is along the chain direction. c,d) Electron density transferred from the CNT to the chain. e) Relative stability of 1D chain phase against 2D monolayer phase and f) magnetic energy of single-chains as a function of electron doping.

an electronic charge transfers from the CNT. The amount of the electron transfer is around 0.25 e per formula unit (f.u.) and does not sensitively depend on the composition. The additional electrons from the CNT are distributed among both transition metal and halide atoms in the chain. Our previous studies also have pointed out that significant charge transfer arises in CNT-encapsulated 1D materials.^[10b,h,18] The charge transfer makes the encapsulating CNTs hole-doped, which can have experimental signatures such as raising of the Raman G band frequency in CNTs.^[19]

To understand the effects of electron doping on MX_3 chains, we calculate the electron doping dependence of MX_3 single-chains in vacuum. Figure 3e compares the total energies of MX_3 in the single-chain phase against the monolayer phase consisting of a honeycomb structure of edge-sharing octahedra. While the monolayer phase is more stable without electron doping, the single-chain phase quickly becomes more stable with electron

doping. When the doping amount is 0.25 e/f.u., which represents the amount of the electron transfer from the CNT, all MX_3 chains are more stable than their monolayer counterparts. This shows that electron transfer from the CNT plays a crucial role in further stabilizing the single-chain phases. For single-chain CrCl_3 synthesized on NbSe_2 substrates, charge transfer may similarly aid stabilization of the chain structure.^[6] In addition, our calculations show that the magnetic states of MX_3 single-chains are strongly affected by electron doping. Figure 3f shows the magnetic energy as a function of electron doping. CrX_3 chains are AFM at the neutral phase but they become FM as electrons are added. Based on the results presented in Figure 3f, the critical doping level for the transition is about 0.35, 0.25, and 0.12 e/f.u. for Cl, Br, and I, respectively.

Therefore, within a CNT with intrinsic charge transfer, the magnetic state of CrI_3 is nominally in the FM state. This doping dependent switching of magnetism for CrX_3 appears in the

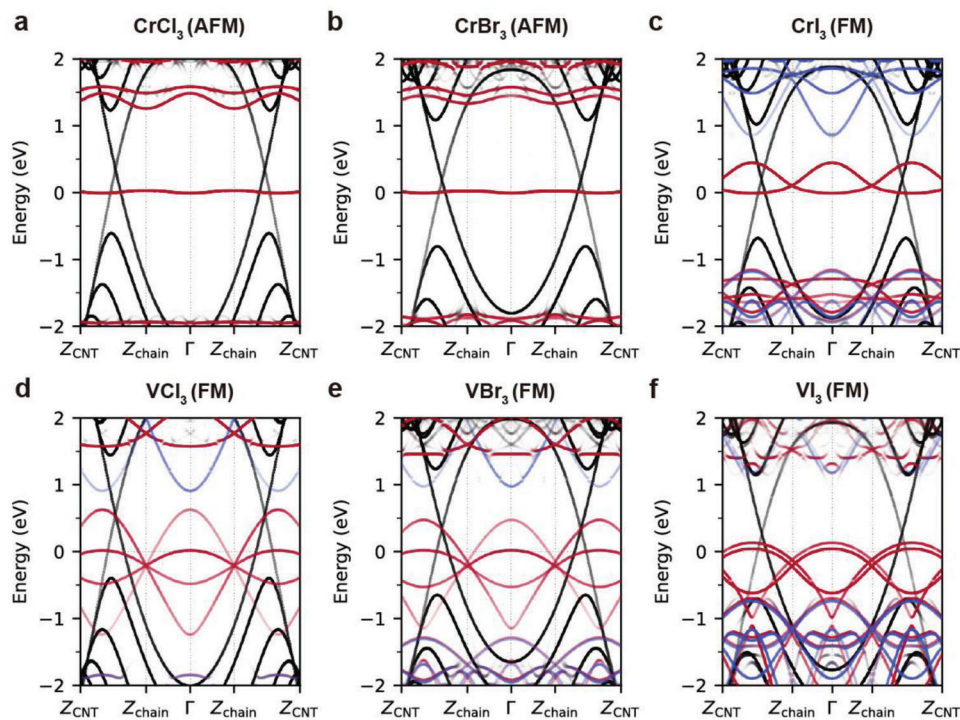


Figure 4. Calculated electronic structures of single-chain MX_3 encapsulated in CNTs. a) Antiferromagnetic CrCl_3 , b) antiferromagnetic CrBr_3 , c) ferromagnetic CrI_3 , and d–f) ferromagnetic VCl_3 , VBr_3 and VI_3 . Supercell band structures are projected onto and unfolded with respect to the primitive Brillouin zone (PBZ) of the chain and CNT, respectively, and Z_{chain} and Z_{CNT} denote the PBZ boundaries. Black lines indicate the CNT states, and red and blue lines are the majority and minority spin states of the chain, respectively.

single-chain phase, but not in its monolayer 2D phase, where the FM ground state is not changed by doping (Figure S10, Supporting Information). On the other hand, the magnetic energy of VX_3 chains also tends to decrease in magnitude with increased doping, but the system remains FM for all doping ranges considered. Our calculations suggest that electrically tunable magnetism in CrX_3 single-chains can be realized by electrostatic gating of CrX_3 -filled CNTs.

Figure 4 shows the electronic structures of MX_3 single-chains encapsulated in CNTs. The Dirac point energy of CNT is pushed upward because of electron transfer from the CNT to the chains. For CrX_3 , electrons transferred from the CNT populate the conduction band of the chain. Notably, with CNT encapsulation, electron doping brings the flat bands in the AFM CrX_3 to the Fermi level, and such states are energetically well separated from the other chain-derived states. Those flat bands can provide an ideal system to study correlated electron physics in 1D. For the FM CrI_3 chain, the additional electron goes into spin-polarized conduction bands, so CrI_3 becomes a half metal. Since the isolated FM VX_3 chains are already half-metallic, charge transfer from the CNT provides additional spin-polarized carriers to the chain.

3. Conclusions

In conclusion, we present 1D CrX_3 and VX_3 magnetic single-chain structures via nanotube encapsulation. We demonstrate the 1D face-sharing octahedron MX_3 structure can be universally synthesized as a single-chain limit inside a nanotube. The nanotube vessel stabilizes and protects the materials, allowing ac-

cess to 1D single-chain limit, specifically CrI_3 , CrBr_3 , CrCl_3 , VI_3 , VBr_3 , and VCl_3 . Our DFT calculations suggest that charge transfer from CNT to MX_3 single-chain plays a critical role in stabilizing the chain structures. Notably, AFM CrX_3 chains host isolated flat bands to which electron doping can be achievable via charge transfer from the CNT. We find that magnetic states of CrX_3 chains can be switched by electron doping. These findings can pave the way for further investigations into low-dimensional magnetic systems and confinement-stabilized materials in nanotubes, which offer exciting opportunities for future research and applications across various fields.

4. Experimental Section

Materials: CNTs were purchased from Sigma Aldrich (single-walled: 704113) and CheapTubes (90% SW-DW CNTs) and were annealed in air at 510 °C for 15 min prior to filling to open the end caps. The precursors utilized for filling included commercially available CrI_3 (purchased from Ossila), CrCl_3 (99.99% Sigma Aldrich and 99.9% Alfa-Aesar), VBr_3 (99.5% Alfa-Aesar), and VCl_3 (99% Alfa-Aesar) powders, as well as synthesized CrBr_3 and VI_3 crystals. The chemical vapor transport (CVT) method was used to grow CrBr_3 and VI_3 precursors. For CrBr_3 , a 1:0.8 molar ratio of Chromium (99% Alfa-Aesar) and TeBr_4 (99.9% Alfa-Aesar) was mixed with a total mass of 1 g in a quartz ampule. For VI_3 , a 1:3 molar ratio of Vanadium (99.7% Alfa-Aesar) and Iodine (99.99% Alfa-Aesar) was mixed with a total mass of 1 g in a quartz ampule. The ampule (10 mm diameter and 15 cm long) was then sealed under high vacuum ($\approx 10^{-6}$ torr) and placed in a horizontal one-zone furnace with the hot end at 750 °C for 5 days before being cooled to room temperature. The synthesized small crystals were extracted inside an Ar-filled glove box to minimize oxidation.

Growing MX₃ @ Nanotube: The CNTs (≈3 mg) were mixed with 30 mg of precursor materials and sealed in a 6 mm inner diameter and 15 cm long quartz ampule under high vacuum (≈10⁻⁶ torr). The sealed ampule was then heated to 650 °C in a single-zone box furnace and kept there for 3 days before being cooled down to room temperature over 1 day. The synthesized materials (MX₃@nanotube) were dispersed in isopropanol using a bath sonicator for 15 min, and drop-cast onto lacey carbon TEM grids for TEM/STEM characterization.

TEM/STEM Imaging and Simulations: Initial sample screening was conducted using a JEOL 2010 microscope at 80 kV. Atomic-resolution ADF-STEM images were acquired using the double spherical (Cs) aberration-corrected JEOL ARM-200F and TEAM 0.5 at the National Center for Electron Microscopy. The JEOL ARM-200F microscopy was set at 80 kV with a 23 mrad convergence angle and collection semiangles ranging from 40 to 160 mrad, while the TEAM 0.5 instrument was operated at 80 kV with a convergence angle of 30 mrad and collection semiangles from 37 to 187 mrad. The electron dose for atomic-resolution STEM imaging was estimated to be ≈ 1 × 10⁸ e⁻ nm⁻². The STEM images were calibrated using 3.4 Å inter-wall spacing of CNTs.

HR STEM image simulations were simulated using MacTempas software based on multislice calculations. The simulation parameters were similar to the experimental parameters (e.g., a probe semiangle of 23 or 30 mrad, 0.05 Å pixel⁻¹ sampling, and 20 frozen phonon calculations) for each simulation. Image analysis and processing were performed using ImageJ software. Poisson noise was added for the simulated STEM images to match the experimental results.

Calculations: First-principles DFT calculations were performed as implemented in SIESTA.^[20] The Perdew–Burke–Ernzerhof functional,^[21] fully relativistic optimized norm-conserving pseudopotentials,^[22] and a localized pseudoatomic orbital basis were used. Van der Waals interactions were included within the Grimme-D2 scheme.^[23] A real-space mesh cut-off of 800 Ry was used. A 40-thick cell was used along the transverse vacuum direction. The primitive Brillouin zone of isolated MX₃ chains was sampled by 32 k points, and the number of k points was proportionally reduced in supercell calculations. The atomic positions of MX₃ chains with and without a CNT were optimized with a force threshold of 0.01 eV Å⁻¹ while fixing the position of carbon atoms in CNT. Electron doping to the isolated chain was simulated by adjusting the total number of electrons and adding positive compensating background charges. The sisl package was used to process and plot the real-space electron density.^[24] For single-chains in CNT, the unfolded band structures were calculated in the same manner as in the previous study.^[10k]

Supporting Information

Supporting Information is available from the Wiley Online Library or from the author.

Acknowledgements

Y.L. and Y.W.C. contributed equally to this work. This work was supported by the US Department of Energy, Office of Science, Basic Energy Sciences, Division of Materials Sciences and Engineering under contract no. DE-AC02-05-CH11231, primarily within the van der Waals Bonded Materials Program (KCWF16) which provided for sample fabrication; within the Nanomachines Program (KC1203) which provided for TEM characterization; and within the Theory of Materials Program (KC2301) which provided theoretical methods and analyses. Computational resources were provided by the DOE at Lawrence Berkeley National Laboratory's NERSC facility and through the Frontera at TACC under Award No. OAC-1818253. Work at the Molecular Foundry (TEAM 0.5 characterization) was supported by the Office of Science, Office of Basic Energy Sciences, of the U.S. Department of Energy under contract no. DE-AC02-05CH11231. K.K. acknowledges support from the Basic Science Research Program at the National Research Foundation of Korea (NRF-2017R1A5A1014862, NRF-2022R1A2C4002559), the Yonsei Signature Research Cluster Program of 2022 (2022-22-0004), the Korea Research Institute of Standards

and Science (KRISS-2023-GP2023-0007), and the Institute for Basic Science (IBS-R026-D1). Y.L. acknowledges support from the Basic Science Research Program at the National Research Foundation of Korea (NRF-2021R1C1C2006785). Y.W.C. acknowledges support from the Basic Science Research Program at the National Research Foundation of Korea funded by the Ministry of Education (RS-2023-00250971).

Conflict of Interest

The authors declare no conflict of interest.

Data Availability Statement

The data that support the findings of this study are available from the corresponding author upon reasonable request.

Keywords

1D materials, atomic chain, density functional theory, magnetic chain, nanotubes, transition metal halide, transmission electron microscopy

Received: August 7, 2023

Revised: September 20, 2023

Published online:

- a) S. A. Wolf, D. D. Awschalom, R. A. Buhrman, J. M. Daughton, S. von Molnár, M. L. Roukes, A. Y. Chtchelkanova, D. M. Treger, *Science* **2001**, 294, 1488; b) P. Gambardella, A. Dallmeyer, K. Maiti, M. C. Malagoli, W. Eberhardt, K. Kern, C. Carbone, *Nature* **2002**, 416, 301; c) C. Gong, L. Li, Z. Li, H. Ji, A. Stern, Y. Xia, T. Cao, W. Bao, C. Wang, Y. Wang, Z. Q. Qiu, R. J. Cava, S. G. Louie, J. Xia, X. Zhang, *Nature* **2017**, 546, 265; d) F. Hellman, A. Hoffmann, Y. Tserkovnyak, G. S. D. Beach, E. E. Fullerton, C. Leighton, A. H. MacDonald, D. C. Ralph, D. A. Arena, H. A. Dürr, P. Fischer, J. Grollier, J. P. Heremans, T. Jungwirth, A. V. Kimel, B. Koopmans, I. N. Krivorotov, S. J. May, A. K. Petford-Long, J. M. Rondinelli, N. Samarth, I. K. Schuller, A. N. Slavin, M. D. Stiles, O. Tchernyshyov, A. Thiaville, B. L. Zink, *Rev. Mod. Phys.* **2017**, 89, 025006; e) B. Huang, G. Clark, E. Navarro-Moratalla, D. R. Klein, R. Cheng, K. L. Seyler, D. Zhong, E. Schmidgall, M. A. McGuire, D. H. Cobden, W. Yao, D. Xiao, P. Jarillo-Herrero, X. Xu, *Nature* **2017**, 546, 270; f) K. S. Burch, D. Mandrus, J.-G. Park, *Nature* **2018**, 563, 47; g) I. Žutić, J. Fabian, S. D. Sarma, *Rev. Mod. Phys.* **2004**, 76, 323.
- a) N. D. Mermin, H. Wagner, *Phys. Rev. Lett.* **1966**, 17, 1133; b) P. A. Lee, N. Nagaosa, X.-G. Wen, *Rev. Mod. Phys.* **2006**, 78, 17.
- a) J.-U. Lee, S. Lee, J. H. Ryoo, S. Kang, T. Y. Kim, P. Kim, C.-H. Park, J.-G. Park, H. Cheong, *Nano Lett.* **2016**, 16, 7433; b) X. Wang, K. Du, Y. Y. Fredrik Liu, P. Hu, J. Zhang, Q. Zhang, M. H. S. Owen, X. Lu, C. K. Gan, P. Sengupta, C. Kloc, Q. Xiong, *2D Mater.* **2016**, 3, 031009.
- M. Bonilla, S. Kolekar, Y. Ma, H. C. Diaz, V. Kalappattil, R. Das, T. Eggers, H. R. Gutierrez, M.-H. Phan, M. Batzill, *Nat. Nanotechnol.* **2018**, 13, 289.
- D. J. O'Hara, T. Zhu, A. H. Trout, A. S. Ahmed, Y. K. Luo, C. H. Lee, M. R. Brenner, S. Rajan, J. A. Gupta, D. W. McComb, R. K. Kawakami, *Nano Lett.* **2018**, 18, 3125.
- S. Lu, D. Guo, Z. Cheng, Y. Guo, C. Wang, J. Deng, Y. Bai, C. Tian, L. Zhou, Y. Shi, J. He, W. Ji, C. Zhang, *Nat. Commun.* **2023**, 14, 2465.
- D. Shcherbakov, P. Stepanov, D. Weber, Y. Wang, J. Hu, Y. Zhu, K. Watanabe, T. Taniguchi, Z. Mao, W. Windl, J. Goldberger, M. Bockrath, C. N. Lau, *Nano Lett.* **2018**, 18, 4214.

- [8] a) J. Zhang, D. Zhao, D. Xiao, C. Ma, H. Du, X. Li, L. Zhang, J. Huang, H. Huang, C.-L. Jia, D. Tománek, C. Niu, *Angew. Chem., Int. Ed.* **2017**, *56*, 1850; b) M. Hart, J. Chen, A. Michaelides, A. Sella, M. S. P. Shaffer, C. G. Salzmann, *Inorg. Chem.* **2019**, *58*, 15216; c) J.-K. Qin, P.-Y. Liao, M. Si, S. Gao, G. Qiu, J. Jian, Q. Wang, S.-Q. Zhang, S. Huang, A. Charnas, Y. Wang, M. J. Kim, W. Wu, X. Xu, H.-Y. Wang, L. Yang, Y. Khin Yap, P. D. Ye, *Nat. Electron.* **2020**, *3*, 141.
- [9] a) R. R. Meyer, J. Sloan, R. E. Dunin-Borkowski, A. I. Kirkland, M. C. Novotny, S. R. Bailey, J. L. Hutchison, M. L. H. Green, *Science* **2000**, *289*, 1324; b) J. Sloan, A. I. Kirkland, J. L. Hutchison, M. L. H. Green, *Chem. Commun.* **2002**, 1319; c) R. Senga, H.-P. Komsa, Z. Liu, K. Hirose-Takai, A. V. Krashennnikov, K. Suenaga, *Nat. Mater.* **2014**, *13*, 1050; d) R. J. Kashtiban, M. G. Burdanova, A. Vasylenko, J. Wynn, P. V. C. Medeiros, Q. Ramasse, A. J. Morris, D. Quigley, J. Lloyd-Hughes, J. Sloan, *ACS Nano* **2021**, *15*, 13389.
- [10] a) A. A. Eliseev, N. S. Falaleev, N. I. Verbitskiy, A. A. Volykhov, L. V. Yashina, A. S. Kumskov, V. G. Zhigalina, A. L. Vasiliev, A. V. Lukashin, J. Sloan, N. A. Kiselev, *Nano Lett.* **2017**, *17*, 805; b) T. Pham, S. Oh, P. Stetz, S. Onishi, C. Kisielowski, M. L. Cohen, A. Zettl, *Science* **2018**, *361*, 263; c) S. Meyer, T. Pham, S. Oh, P. Ercius, C. Kisielowski, M. L. Cohen, A. Zettl, *Phys. Rev. B* **2019**, *100*, 041403; d) C. A. Slade, A. M. Sanchez, J. Sloan, *Nano Lett.* **2019**, *19*, 2979; e) M. Nagata, S. Shukla, Y. Nakanishi, Z. Liu, Y.-C. Lin, T. Shiga, Y. Nakamura, T. Koyama, H. Kishida, T. Inoue, N. Kanda, S. Ohno, Y. Sakagawa, K. Suenaga, H. Shinohara, *Nano Lett.* **2019**, *19*, 4845; f) T. Pham, S. Oh, S. Stonemeyer, B. Shevitski, J. D. Cain, C. Song, P. Ercius, M. L. Cohen, A. Zettl, *Phys. Rev. Lett.* **2020**, *124*, 206403; g) S. Stonemeyer, J. D. Cain, S. Oh, A. Azizi, M. Elasha, M. Thiel, C. Song, P. Ercius, M. L. Cohen, A. Zettl, *J. Am. Chem. Soc.* **2021**, *143*, 4563; h) J. D. Cain, S. Oh, A. Azizi, S. Stonemeyer, M. Dogan, M. Thiel, P. Ercius, M. L. Cohen, A. Zettl, *Nano Lett.* **2021**, *21*, 3211; i) S. Stonemeyer, M. Dogan, J. D. Cain, A. Azizi, D. C. Popple, A. Culp, C. Song, P. Ercius, M. L. Cohen, A. Zettl, *Nano Lett.* **2022**, *22*, 2285; j) W. J. Cull, S. T. Skowron, R. Hayter, C. T. Stoppiello, G. A. Rance, J. Biskupek, Z. R. Kudrynskiy, Z. D. Kovalyuk, C. S. Allen, T. J. A. Slater, U. Kaiser, A. Patanè, A. N. Khlobystov, *ACS Nano* **2023**, *17*, 6062; k) Y. Lee, Y. W. Choi, K. Lee, C. Song, P. Ercius, M. L. Cohen, K. Kim, A. Zettl, *ACS Nano* **2023**, *17*, 8734.
- [11] a) R. J. Kashtiban, C. E. Patrick, Q. Ramasse, R. I. Walton, J. Sloan, *Adv. Mater.* **2023**, *35*, 2208575; b) M. Gao, Y. Park, J. Jin, P.-C. Chen, H. Devyldere, Y. Yang, C. Song, Z. Lin, Q. Zhao, M. Siron, M. C. Scott, D. T. Limmer, P. Yang, *J. Am. Chem. Soc.* **2023**, *145*, 4800.
- [12] E. Drent, C. A. Emeis, A. G. T. G. Kortbeek, *Chem. Phys.* **1975**, *10*, 313.
- [13] J. M. Fletcher, W. E. Gardner, A. C. Fox, G. Topping, *J. Chem. Soc. A* **1967**, 1038.
- [14] a) D. I. Khomskii, K. I. Kugel, A. O. Sboychakov, S. V. Streltsov, *J. Exp. Theor. Phys.* **2016**, *122*, 484; b) K. I. Kugel, D. I. Khomskii, A. O. Sboychakov, S. V. Streltsov, *Phys. Rev. B* **2015**, *91*, 155125.
- [15] a) J. L. Lado, J. Fernández-Rossier, *2D Mater.* **2017**, *4*, 035002; b) C. Bacaksiz, D. Šabani, R. M. Menezes, M. V. Milošević, *Phys. Rev. B* **2021**, *103*, 125418.
- [16] a) A. I. Liechtenstein, M. I. Katsnelson, V. P. Antropov, V. A. Gubanov, *J. Magn. Magn. Mater.* **1987**, *67*, 65; b) X. He, N. Helbig, M. J. Verstraete, E. Bousquet, *Comput. Phys. Commun.* **2021**, *264*, 107938.
- [17] Z. P. Yin, K. Haule, G. Kotliar, *Nat. Mater.* **2011**, *10*, 932.
- [18] a) D. Popple, M. Dogan, T. V. Hoang, S. Stonemeyer, P. Ercius, K. C. Bustillo, M. Cohen, A. Zettl, *Phys. Rev. Mater.* **2023**, *7*, L013001; b) C. Chen, J. Avila, S. Wang, Y. Wang, M. Mucha-Kruczyński, C. Shen, R. Yang, B. Nosarzewski, T. P. Devereaux, G. Zhang, M. C. Asensio, *Nano Lett.* **2018**, *18*, 1082.
- [19] A. M. Rao, P. C. Eklund, S. Bandow, A. Thess, R. E. Smalley, *Nature* **1997**, *388*, 257.
- [20] J. M. Soler, E. Artacho, J. D. Gale, A. García, J. Junquera, P. Ordejón, D. Sánchez-Portal, *J. Phys.: Condens. Matter* **2002**, *14*, 2745.
- [21] J. P. Perdew, K. Burke, M. Ernzerhof, *Phys. Rev. Lett.* **1996**, *77*, 3865.
- [22] D. R. Hamann, *Phys. Rev. B* **2013**, *88*, 085117.
- [23] S. Grimme, *J. Comput. Chem.* **2006**, *27*, 1787.
- [24] N. Papior, P. Febrer, T. Frederiksen, N. Wittemeier, A. Kole, sisl: v0.13.0, <https://doi.org/10.5281/zenodo.7567793> (accessed: April 2023).